PETROLOGICAL STUDY OF THE RONDA PERIDOTITE USING AVIRIS IMAGES AND FIELD MEASUREMENTS: CALIBRATION AND RELIEF CORRECTIONS

Patrick Launeau and Daniela Despan

Laboratoire de Planétologie et Géodynamique,
2, rue de la Houssinière, BP 92208, 44322 Nantes, France
(Patrick.Launeau@chimie.univ-nantes.fr)
(Daniela.Despan@chimie.univ-nantes.fr)

1. Introduction

The Ronda Peridotite, SW of Spain, was imaged by AVIRIS in 1991 and partially sampled in the field with a GER 3700 spectrometer in 1997 in order to get experience in processing multispectral images of planetary surfaces. On Earth, it is also necessary to determine species of vegetation because of their strong influence in mapping rock types, even in dry area like for the Ronda peridotite. However, the Ronda peridotite is a good training site. It displays a complex rock type zoning acquired along geological time (Lundeen and Obata 1977), from its petrogenesis to its superficial alteration.

We calibrate the 1991 AVRIS image with field measurements made in 1997. Because of topographic effect, we use spectral angle mapping techniques for comparison between image and field measurements. However, since the peridotite types of Ronda have close mineral compositions (compare harzburgite and lherzolite), their spectra are similar to each and thus difficult to identify with angle mapping techniques. Moreover, because of the partial coverage of the peridotite by different plants, and because the effect of slope orientation and roughness, we want to outline in this work the need of BRDF modelling in order to identify all the component of the image and improve geological mapping.

2. Petrology

The Ronda peridotite massif outcrops in the southern part of Spain at the latitude of about N 36° in a Mediterranean climate (Figure 1). It expresses a slice of the mantle that was uplifted during the alpine orogeny (Dewey et al., 1989). The peridotite is now in tectonic contact with continental metamorphic series of the Betic Cordilleras that dominantly comprise metapelitic rocks (gneisses and schists) and marbles of Paleozoic to Triassic ages (see precise descriptions of these lithologies in Tubia et al., 1992, 1997). The main mineral phase of the Ronda peridotite massif is olivine, which modal composition varies from more than 90% in dunites down to 65% in lherzolites. However, 30 to 90% of this primary mineral is now transformed into serpentines and magnetite. The second mineral phases of the Ronda peridotite are pyroxenes which can be divided into clinopyroxene (cpx) and

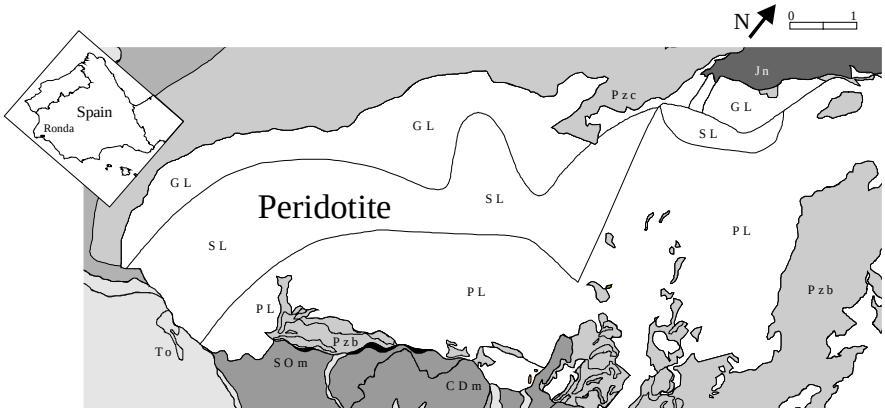

Figure 1
Geological map from Lundeen and Obata 1977.

Ronda Peridotite types:
GL - garnet lherzolite
SL - spinel lherzolite
PL - plagioclase lherzolite
Jn jurassic limestone
To, oligocene sandstone
Others are metamorphic rocks.

orthopyroxene (opx), equally distributed within the lherzolites, whereas opx dominates in harzburgite. The Ronda peridotite also locally comprises layers 10cm to 2m thick of pyroxenites (usually 100% cpx) and of rare olivine

gabbros. The modal content of all the other phases present in these peridotites is always very low : around 1% for plagioclase, between 1 and 3% for spinel and less than 1% for garnet.

3. Field measurement

We use the GER 3700 spectrometer. It analyses the light between 300 and 2500 nanometer in three contiguous windows defined by one CCD and two PbS. For each sample of the field, a white reference is measured on a white spectralon. Then, the sample itself is measured and can be compared to the white reference. We call DN(i, λ) the count of photon for the sample i and DN(i*, λ) its corresponding white reference for each wavelength λ. By using GER factory calibration, each DN spectra is converted in spectra of radiance R(i, λ) and R(i*, λ). Then, the reflectance is given for each λ by the ratio :

$$\rho(i,\lambda) = R(i, \lambda) / R(i^*, \lambda) \quad (\mathbf{1})$$

For comparison with other spectra, which may have been measured on surfaces having different slopes, it is convenient to calculate the normalized reflectance ρ_n by dividing each value of a spectrum by its mean value :

$$\overline{\rho} = \frac{1}{n} \sum_{\lambda=400}^{1800} \rho(i,\lambda) \quad (\mathbf{2a})$$

$$\rho_n(i,\lambda) = \rho(i,\lambda) / \overline{\rho} \quad (\mathbf{2b})$$

ρn is not sensitive to the topography. 740 spectra have been acquired on the Ronda peridotite Massif and a few location around it. A selection of spectra of the peridotite are presented in Annexe.

4. Image calibration

Like previous authors working on the AVIRIS data of the Ronda peridotite (Chabrillat, 1995) we use the classical empiric line correction (Roberts et al. 1986; Kruse et al., 1990; Richards, 1994; Farrand et al. 1994). This process, applied to each wavelength channel, requires black and white control points which where identified on the colour composition images of Figure 1c displaying the minimum, mean and maximum values of each spectrum on red, green and blue channels respectively.

$$R(x,y,\lambda) = R(b,\lambda) + \mathbf{(}\ DN(x,y,\lambda) - DN(xb,yb,\lambda)\ \mathbf{)}\cdot C(\lambda) \quad (\mathbf{3})$$

with $$C(\lambda) = \frac{R(b^*,\lambda) - R(b,\lambda)}{DN(xw,yw,\lambda) - DN(xb,yb,\lambda)} \quad (\mathbf{4})$$

Since the white control point is a perfect reflection of the sun light (its radiance spectra is equal to the radiance spectra of a spectralon), we can calculate the reflectance as:

$$\rho(x,y,\lambda) = R(x,y,\lambda) / R(xw,yw,\lambda) \quad (\mathbf{5})$$

The validity of this calculation has been tested on various control points presented below. This absolute reflectance should not be confused with the apparent reflectance r:

$$r(x,y,\lambda) = DN(x,y,\lambda) / DN(xb,yb,\lambda) \quad (\mathbf{6})$$

We have lost a lot of time trying to understand its information contain. A lake of calibration do not allows the right identification of the atmosphere contribution. By working on absolute reflectance ρ, we can identify the atmosphere with the following index (Figure 2a):

$$I_e(x,y) = 2\,\rho(x,y,948) / (\rho\,(x,y,920) + \rho\,(x,y,968)) \quad (\mathbf{7})$$

A digital elevation model (DEM) can be produced using a regression line between I_e values and heights of a few locations ($H(x,y) = a \,.\, (I_e(x,y) - b)$ and the resulting DEM is presented in Figure 3e).

Similarly to Green et al. (1989) and Gao et al. (1993) we calculate the contribution of the atmosphere with the following ratio of two spectralon measurements at 350m and 1400m (Figure 2b):

$$AF(\lambda) = \frac{R(\text{site at } 350\text{m}^*, \lambda)}{R(\text{site at } 1400\text{m}^*, \lambda)} - 1 \qquad \textbf{(8)}$$

However, Because of variations along season (Roberts et al. 1997) it is also required to collect it during the same season, even a few years apart. This was done in July 97 in two sites around noon, less than two hours apart from each other during the same day, but six years after the AVIRIS acquisition in 1991.

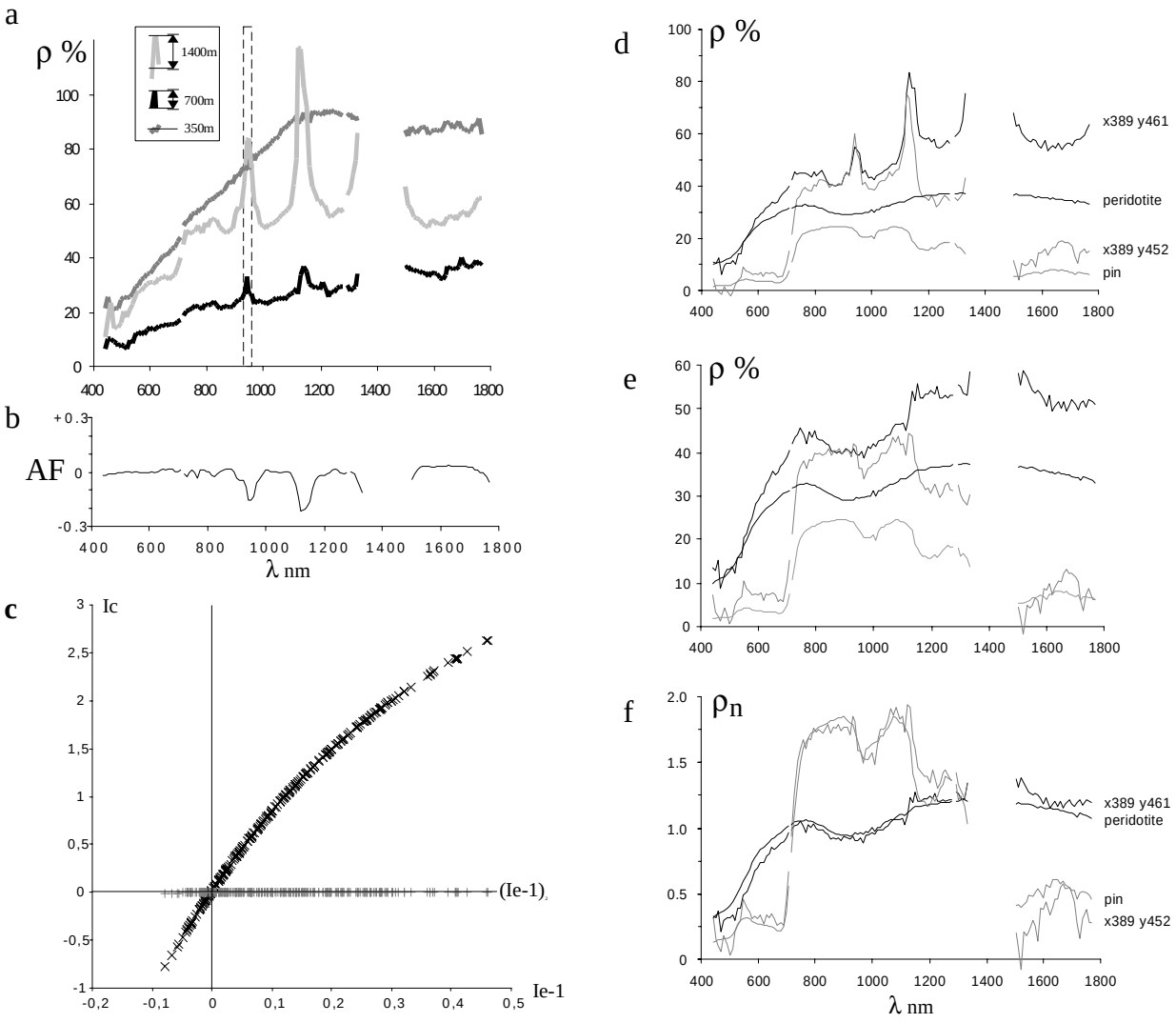

Figure 2: Correction of the atmosphere. **a**- reflectance spectra calibrated at 350m. **b**- ratio between spectralon measurement at 350m and 1400m. c- calculation of Ic (see texte). **d**- comparison between AVIRIS data and field measurements. **e**- same comparison after atmosphere correction. **f**- same comparison with normalized refectance.

The effect of the atmosphere vary with height and water vapor density, so an other transformation should be used in order to remove it.

$$\rho_a(x,y,\lambda) = \rho\,(x,y,\lambda) \cdot \{1 + (AF(\lambda) \cdot Ic(x,y))\} \quad (\mathbf{9})$$

with $$I_c(x,y) = 0.1588 \,.\, (I_e(x,y)\text{-}1)^4 + 6.7184 \,.\, (I_e(x,y)\text{-}1)^3 - 11.035 \,.\, (I_e(x,y)\text{-}1)^2 + 9.3197 \,.\, (I_e(x,y)\text{-}1) - 0.0159 \quad (\mathbf{10})$$

Ic was determined at various altitude and compared to Ie. The polynomial function is used to apply the transformation to the whole image. It allows to remove all the artefacts produced by the height discrepancy between any pixel and the white reference taken at 350m as it is well evidenced between Figure 2d and 2d.

5. Spectral angle mapping

Similarly to Van de Meer (1996) we look at correlation coefficient between field and airborne measurements. We use the following spectral angle mapping (SAM) defined by Kruse et al. (1993) to compare each pixel (x,y) with a sample j :

$$\text{Angle}(x, y, j) = \cos^{-1}\left(\frac{\sum_\lambda \rho(x, y, \lambda) \cdot \rho(j, \lambda)}{\sqrt{\sum_\lambda \rho(x, y, \lambda)^2} \cdot \sqrt{\sum_\lambda \rho(j, \lambda)^2}} \right) \quad (\mathbf{11})$$

and to built the channel j of an image of spectral angle mapping with :

$$I_a(x,y,j) = 1000 \,/\, \text{Angle}(x,y,j) \quad (\mathbf{12})$$

with I_a being a short integer more suitable to code images (2 bytes / pixel). I_a is not sensitive to slope angle and variations of intensity (Kruse et al., 1993). The same calculation using ρ_n instead of ρ gives exactly the same result, it only compares shape of spectra. When ρ_n is available, one can substitute the usual equation 15 by the following equation 17 which returns quite the same result but which is a lot faster to obtain on a personal computer.

$$D(x, y, j) = \frac{1}{n} \sum_\lambda \frac{\rho_n(x, y, \lambda) - \rho_n(j, \lambda)}{\rho_n(j, \lambda)} \quad (\mathbf{13})$$

with the corresponding image given by I_d:

$$I_d(x,y,j) = 1000/D(x,y,j) \quad (\mathbf{14})$$

Both calculations were applied to various sites with comparison to harzburgite in Figure 3.

The maps of index I_d for harzburgite (Figure 3b) and lherzolite display some variation inside the peridotite. However, those variation are oblique on geological boundary. In fact, the comparison is very difficult because of the vegetation cover. The colour composition of Id maps of harzburgite, grass and thistle shown in red, green and blue channel respectively (Figure 3c), shows that harzburgite (like other peridotite types) are largely covered by various plants. An extension of peridotite mapping imply to remove the vegetation coverage which change from slope to slope (see Figure 3f and 3h). For this, we envisage to use vegetation modelling (see Jacquemoud, 1993; Elvidge et al. 1993).

The use of normalised reflectance, and spectral angle mapping, minimise the segregation between rock types (Figure 2f). This segregation is enhanced with absolute reflectance but it can change a lot with slope orientation. A better mapping of the peridotite definitely required to analyse the effect of the topography in order to use the full information of absolute reflectance.

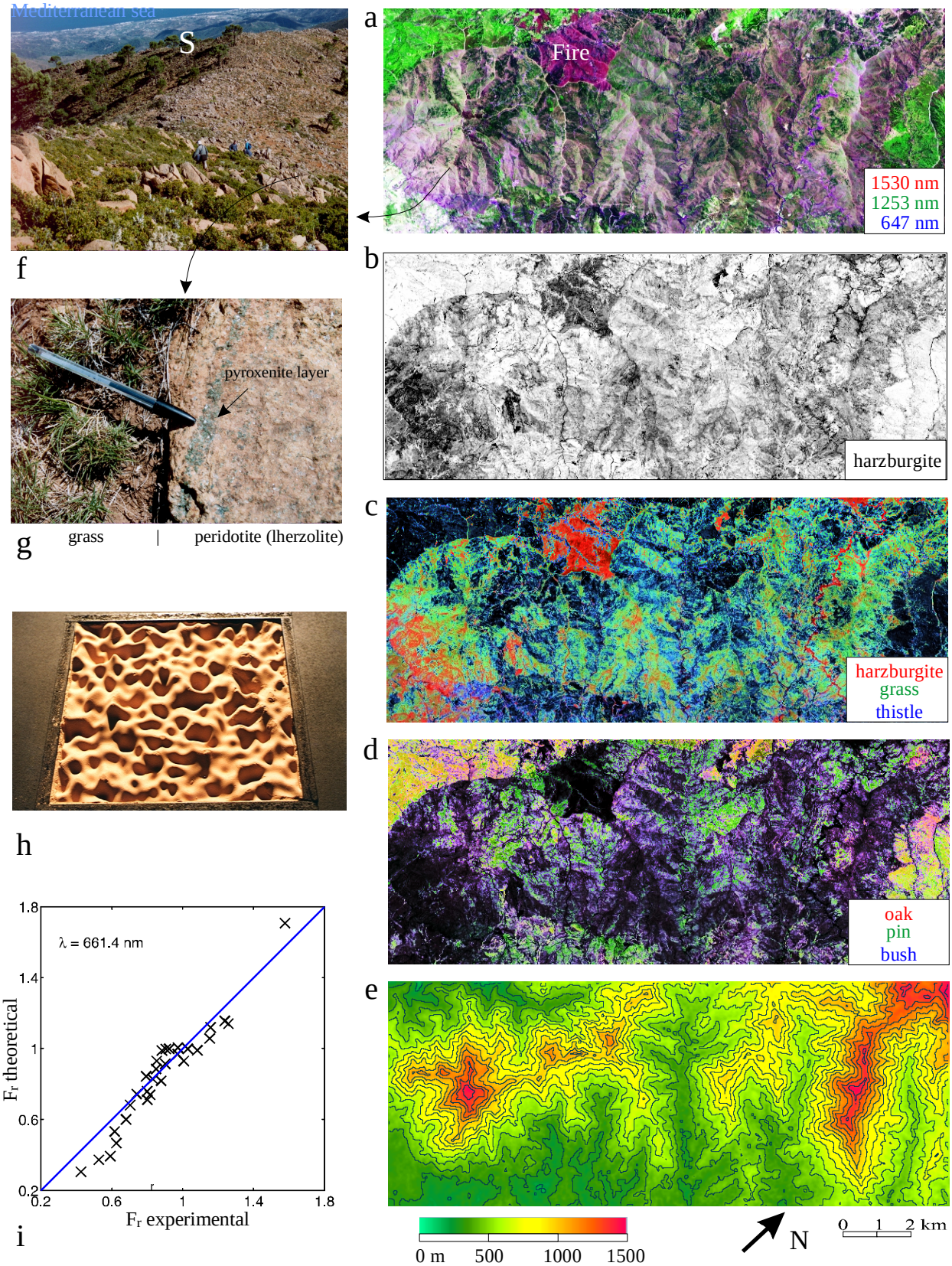

Figure 3: Colour plate. **a**- spectral colour composition; **b**- Id map; **c-d**- Id map colour compositions; **e**- DEM based on I_e calculation; **f**- view from the Reales Mount; **g**- detail of f; **h**- model of topography (sand); **i**- validation (see §6).

6. Topography

A BRDF model for random rough surfaces using probabilistic expression for the shadowing factor and the conditional mean slope was previously proposed (Despan et al., 1998, 1999). The surface is represented by a Gaussian process, characterised by its autocorrelation length L and root mean square (rms) of the height σ_h. The BRDF of the rough surface is:

$$R_r = \frac{1}{A_0 \cos\theta_e^0} \int \Phi(P) R_s(\theta_i(P), \theta_e(P), \varphi(P)) \frac{\cos\theta_e(P)}{\cos\theta(P)} dA_0(P), \quad (\mathbf{15})$$

θ_e^0 is the emergence angle, (with respect to the normal to the mean plane of the surface). $\theta_e(P)$ and $\theta_i(P)$ are the angles between the emergence and incidence directions and the normal at a point P. $\varphi(P)$ is the angle between the incidence and the emergence planes at P. $\theta(P)$ is the angle between the normal to the mean plane and the normal at P. A_0 and $dA_0(P)$ are the total projected area and the projected area element on the mean plane. $\Phi(P)$ is the shadowing function. R_s represents the BRDF of a planar smooth facet. By using the ergodic theorem and the total expectation formula, it follows:

$$R_r = \frac{1}{\cos\theta_e^0} P[\Phi = 1] R_s\left(\theta_i^{eff}, \theta_e^{eff}, \varphi^{eff}\right) \cos\theta_e^{eff} \quad (\mathbf{16})$$

$$\sin\theta_{i,e}^{eff} = \frac{E[h_x | \Phi = 1] \cos\theta_{i,e}^{eff} + \sin\theta_{i,e}^{eff}}{\sqrt{1 + \left(E[h_x | \Phi = 1]\right)^2}} \quad (\mathbf{17})$$

$\sin\theta_{i,e}^{eff}$ is the effective angle in the case of coincident incident and emergent planes.

$E[h_x | \Phi = 1]$ is the conditional mean slope which is the average slope on the parts of the surface that are both illuminated and visible.

$P[\Phi = 1]$ is the shadowing factor which is the probability that a point is illuminated and visible.

We proceeded to numerical simulations to improve the analytical expression of these two quantities. In order to validate this model, we used the European Goniometric Facility (EGO) of the Joint Research Centre at Ispra, Italy, equipped with the SE590 spectroradiometer (400-1100 nm range) and a halogen source. We have used different types of soils as target. Diffused light was measured for different elevations of the source and for each source position for a set of different elevations and azimuths of the detector. The model is valid for various types of soils (Figure 3h and 3i). We have defined the roughness factor as ratio of the BRF, Bidirectional Reflectance Factor, of the rough surface to the one for the smooth surface.

We now have to measure those parameters on the Ronda peridotite. We will focus our study, next June, on the southern part of the massif (see Figure 3a-c) where the peridotite is better exposed.

The usefulness of the BRDF model concerns the application where we need to make a difference between minerals with similar shapes of spectra but different absolute values of intensities. Bidirectional information should be also used. For this, we intent to collect birectional measurements on ground for the Ronda site. To compared ground and satellite spectra, one needs topographical information of the local inclination for each pixel or for a group of similar pixels.

The reflectance model we developed and validated, allows to connects statistics of inclinations and statistics of values of the reflectance. Also we may try to use the information on reflectance to get the inclination of pixels and draw a topographical model of the region (provided that we have information on the distribution of minerals).

7. Conclusion-perspectives

We expect to use BRDF model to remove the effect of the topography on the Ronda peridotite. The analysis of the vegetation cover will allows to built a model and remove its contribution since its coverage often do not excess 60%. The ability of the angle mapping technique to map various plants on the peridotite should facilitate this process. The large variation of absolute reflectance between peritotite types should also produces very well contrasted maps of I_d indexes.

References

Chabrillat S., 1995, "Discrimination lithologique par spectro-imagerie visible-proche infrarouge aéroportée: application au Massif péridotitique de Ronda (Espagne)", Dr. Thesis Univ. Toulouse 3, 173 pp.

Despan, D., Bedidi, A., Cervelle, B., Rudant, J. P. , 1998, "Bidirectional Reflectance of Gaussian Random Surfaces and its Scaling Properties". Math. Geo. 30, pp. 873-888.

Despan, D., A., Bedidi, B., Cervelle, 1999, "Bidirectional Reflectance of rough bare soil surface" Geophysical Research Letters, Vol. 26, No 17, 2777-2780

Dewey J.F., Helman M.L., Turco E., Hutton DWH., Knott SD., 1989, "Kinematics of the western Mediterranean", In : Coward MP., Dietrich D., Park RG (Eds), Alpine Tectonics. Geol. Soc. London Spec. Publ. 45, 265-283.

Elvidge C. D., Z. Chen and D. P. Groeneveld, 1993, "Detection of Trace Quantities of Green Vegetation in 1990 AVIRIS Data", Remote Sen. Environ. 44, pp. 271-279.

Farrand W. H., R. B. Singer, and Erzsébet Merényi, 1994, "Retrieval of Apparent Surface Reflectance from AVIRIS Data: A comparison of Empirical Line, Radiative Transfer, and Spectral Mixture Methods", Remote Sens. Environ. 47, pp. 311-321.

Gao B.-C., K. B. Heidebrecht, and A. F. H. Goetz, 1993, "Derivation of Scaled Surface Reflectances from AVIRIS Data", Remote Sens. Environ, 44, pp. 165-178.

Green R. O., V. Carrere, and J. E. Conel, 1989, "Measurement of atmospheric water vapor using the Airborne Visible/Infrared Imaging Spectrometer". Image Processing '89, American Society for Photogrammetry and Remote Sensing (ASPRS).

Jacquemoud S., 1993, "Inversion of the PROSPECT + SAIL Canopy Reflectance Model from AVIRIS Equivalent Spectra: Theoretical Study", Remote Sens. Environ. 44, pp. 281-292.

Kruse F. A., K. S. Kierein-Young and J. W. Boardman, 1990, "Mineral mapping at cuprite, Nevada with a 63-channel imaging spectrometer", Photogramm. Eng. Remote Sens. 56 (1), pp. 83-92.

Kruse F. A., A. B. Lefkoff, J. W. Boardman, K. B. Heidebrecht, A. T. Shapiro, P. J. Barloon, and A. F. H. Goetz., 1993, "The Spectral Image Processing System (SPIS) - Interactive Visualization and Analysis of Imaging Spectrometer Data", Remote Sens. Environ, 44, pp. 145-163.

Lundeen M. T. and M. Obata, 1977, "Geologic map of the Ronda ultramafic complex, southern Spain", The Geological Society of America, Inc. © 1979, Map and chart series MC-29.

Richards J. A., 1994, "Remote Sensing Digital Image Analysis: An Introduction, Second, Revised and Enlarged Edition". Springer-Verlag, 340pp.

Roberts D. A., Yamagushi Y. and R. J. P. Lyon, 1986, "Comparison of various techniques for calibration of AIS data", in Proc. 2nd Airborne Imaging Spectrometer Data Analysis Workshop (G. Vane and A. F. H. Goetz, Eds.)

Roberts D. A., R. O. Green and J. B. Adams, 1997, "Temporal and Spatial Patterns in Vegetation and Atmospheric Properties from AVIRIS", Remote Sens. Environ. 62, pp. 223-240.

Tubía J. M., J. Cuevas, J., Navarro-Vila, F., Alvarez, F., Aldaya, 1992, "Tectonic evolution of the Alpujarride complex (Betic Cordilleras, Southern Spain)", J. Struct. Geol. 14, pp. 193-203.

Tubía J. M., J. Cuevas and JI. Gil Ibarguchi, 1997, "Sequential development of the metamorphic aureole beneath the Ronda peridotites and its bearing on the tectonic evolution of the Betic Cordillera", Tectonophysics 279, pp. 227-252.

Van Der Meer F., 1996, "Metamorphic facies zonation in the Ronda peridotites: spectroscopic results from field and GER imaging spectrometer data", Int. J.Remote Sensing, 1996, vol. 17, no. 9, pp. 1633-1657.

APPENDIX

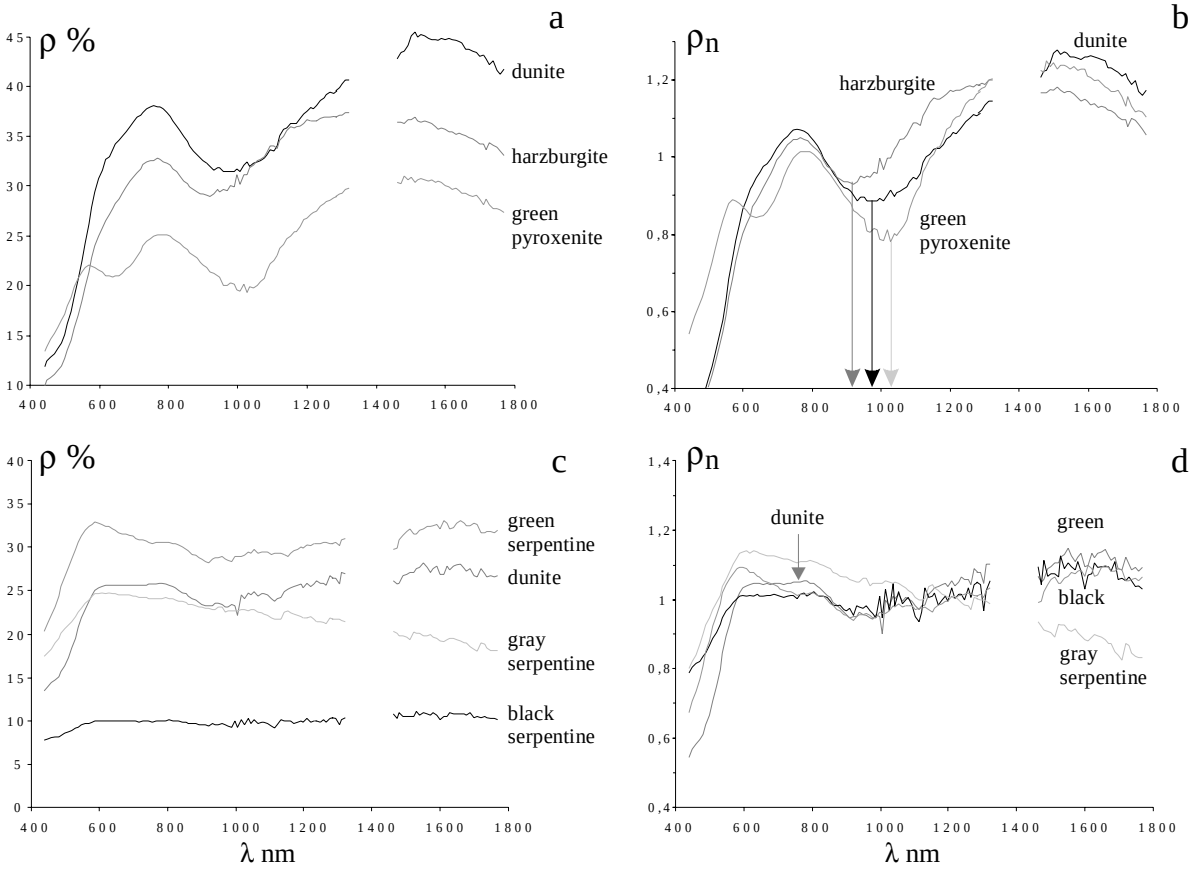

Figure A1: collection of absolute reflectance (a, c) and normalise reflectance (b, d). a- peridotite types. b- the same peridotite types are closer to each other in normalised reflectance orthopyroxene (opx) and clinopyroxene (cpx) can be detected. c- colelction of serpentine for comparison with serpentinized peridotite (dunite). d- same collection showing that serpentines are more difficult to distinguish from each other with normalised reflectance.